International Journal of Precision Engineering and Manufacturing-Green Technology (2023) 10:85–96
https://doi.org/10.1007/s40684-022-00418-y

Online ISSN 2198-0810
Print ISSN 2288-6206

REGULAR PAPER

# One-Step Fabrication of Superhydrophobic Surfaces with Wettability Gradient Using Three-Dimensional Printing

**Jaebum Sung[1] · Hoo Min Lee[1] · Gil Ho Yoon[1] · Sungchul Bae[2] · Hongyun So[1,3]**

Received: 8 September 2021 / Revised: 23 November 2021 / Accepted: 4 January 2022 / Published online: 22 February 2022


## Abstract

Polymer surfaces with wettability gradient were fabricated using three-dimensional (3D) printing technology to control the velocity of droplets on the surfaces. A microscale pattern of a semicircular casting mold was created layer-by-layer using a 3D printer based on fused deposition modeling. A surface with a wettability gradient was fabricated by replicating the semicircular mold with a continuously varying surface slope. Water contact angle measurements and droplet test results demonstrated the characterization of the wettability gradient. Droplets were released on a gradient surface inclined at 80°, and their movements were controlled; the locations of the droplets after collision on the ground were tracked. The distance of the main drop and splash drop was found to be reduced by 96.7% (from 6.1 to 0.2 cm) and 87.8% (from 18.8 to 2.3 cm), respectively, compared to that on a general superhydrophobic surface. This study demonstrates a simple, rapid, and inexpensive microfabrication method for functional polymer surfaces to control droplet movement using 3D printing technology.

**Keywords** Wettability gradient · Superhydrophobic · 3D printing · Rapid prototyping · Droplet control

## 1 Introduction

Numerous functional surfaces have been studied within different fields for a variety of purposes. In nature, typical examples of these surfaces include superhydrophobic lotus leaves [1, 2], rose petals with high adhesion [3, 4], and sharkskin, a material that reduces hydraulic resistance [5, 6]. New methods are now being used to artificially mimic and create functional surfaces such as optical surfaces [7, 8], surfaces with hydrophobicity [9, 10], and surfaces that separate water and oil [11, 12]. Wettability gradient surfaces, which are also functional surfaces, are being researched extensively in the microfluidics [13–15] and biomedical [16, 17] fields, and they can be fabricated with various ranges of wettability between superhydrophobicity and superhydrophilicity. To date, conventional wettability gradient surfaces have been fabricated using lasers [18–20], chemicals [21–24], temperature gradient methods [25–27], electrochemical techniques [28, 29], morphological techniques [30–32], plasma [33], photodegradation [34], and vibration [35], but these methods involve expensive equipment and require complex processes, such as a clean room for precise manufacturing.

Three-dimensional (3D) printing technology has similarly gained recent popularity within a range of fields and can produce structures of various sizes, from real-scale to nanoscale [36, 37]. In particular, the fused deposition modeling (FDM)-type 3D printers have provided considerable experimental data for microscale projects, and products directly manufactured by the FDM-type 3D printing method, as well as their polymer duplicates, have been used in recent studies. The items produced by FDM-type 3D printers differ depending on nozzle diameter [38, 39], printing direction [40], bottom layer line width [41], nozzle temperature [42–44], and other printing parameters. The surface roughness of the product is affected by the height of the layer [45] and the printing angle [46]; it is also related to the wettability of the product. In general, a large layer height and large printing angle lower the wettability from hydrophobic to superhydrophobic; however, when only the tilting angle is changed at the same printing resolution (i.e., the height of the layer), the wettability changes continuously with the angle. This feature can be utilized to design

✉ Hongyun So
hyso@hanyang.ac.kr

[1] Department of Mechanical Engineering, Hanyang University, Seoul 04763, South Korea

[2] Department of Architectural Engineering, Hanyang University, Seoul 04763, South Korea

[3] Institute of Nano Science and Technology, Hanyang University, Seoul 04763, South Korea

a semicircular mold that continuously increases the surface angle, and a surface with a wettability gradient can be fabricated. This study demonstrates the use of a simple, rapid, and cost-effective microfabrication of a functional polymer surface to control the wettability gradient and hence the velocity of a droplet rolling off the surface. A computer-aided design (CAD) program was used to construct molds of this velocity control surface (VCS) in various sizes, which were then analyzed by measuring the water contact angle (WCA) and conducting a droplet test to successfully obtain the characteristic of the VCS. Further velocity experiments and splash tests demonstrated the remarkable control of droplets on these surfaces compared to those on conventional superhydrophobic surfaces and flat polymer surfaces. The results of this study will facilitate the use of FDM-type 3D printing technology in the microfluidics field and for environmental applications, where a rolling droplet's speed needs to be controlled.

## 2 Experimental Section

### 2.1 Materials

Previous studies have proved that the surface spacing, the pattern of the manufactured mold, and the wetting properties of a mold's polymer cast differ based on the printing angle. Therefore, a surface with varied wettability (i.e., gradient) was fabricated by continuously changing the printing angle of a semicircular mold designed using a CAD program (NX 11, Siemens). The schematic in Fig. 1 shows the construction of the VCS. Polylactic acid (PLA) filaments (Ø1.75 mm) in an FDM-type 3D printer (GUIDER IIs, Flashforge, China) were used to construct the semicircular mold (Fig. 1a); the surface of this mold exhibited gradient roughness (angle) owing to the inherent characteristics of the FDM-type printer, as shown in the inset of Fig. 1a. This gradient roughness determined the gradient structures and hence the surface's wettability. The 3D printing setup had a layer height of 0.4 mm, a stage temperature of 50 °C, and an extruder temperature of 220 °C. Three different semicircle radii (i.e., 3, 4, and 5 cm) were characterized for this study. Following this, a polydimethylsiloxane (PDMS, Sylgard 184, Dow Corning Inc.) mixture (prepolymer:curing agent = 10:1) was poured into the bottom mold, and the top mold was inserted (Fig. 1b). Because the semicircular mold had the gradient surface angle in the range of 0°–90°, the PDMS surface cast from the printed mold exhibited the same gradient angle of structures, as shown in the inset of Fig. 1b. The gap between the two molds was designed to produce a 2-mm-thick polymer layer. Air bubbles were removed by a 2-h degassing process in a vacuum chamber (Fig. 1c), followed by the polymerization of the PDMS mixture on a hot plate at 50 °C for 8 h (Fig. 1d). The cured polymer was then demolded by bathing it in acetone for 12 h (Fig. 1e). The side surfaces of semicircular polymer cast from the mold were removed to separate the patterned surface only (Fig. 1f), and the patterned layer was flattened by applying epoxy (2-ton epoxy, ITW DEVCON) on the flat bed, followed by pressing and flattening for 2 h to finalize the surface (Fig. 1g). The stretched semicircular polymer surface had different wettability characteristics (i.e., gradation from hydrophobicity to superhydrophobicity), enabling the speed control of the droplets (Fig. 1h).

### 2.2 Testing and Characterizations

#### 2.2.1 Static Water Contact Angle Analysis

For the verification of the wettability gradation of the fabricated surface, the semicircular polymer was divided into nine sections of uniform distances, from its center to its end. The WCA of the surface was measured at equal intervals, denoted by P1–P8 (see Fig. 1g), where each position was assumed to be 10º apart. A WCA goniometer (Phoenix-MT(A), Surface Electro Optics, Korea) and an image conversion software (Image Pro 300) were used to measure the WCA with a ~ 7-µl droplet. The WCA was calculated as the average of five values measured using the tangent line method [47, 48].

To evaluate the characteristics of the measured perpendicular WCA, the Cassie-Baxter and the Wenzel models were applied and theoretically analyzed. The Young's contact angle ($\theta_Y$) used in both models was ~ 107° [49], which is the WCA on the smooth PDMS surface. A rough surface (e.g., nano/micropatterned surface) affects wettability by large and small steps on the surface, and the analysis method is different depending on the wetting state. When the droplet was in a complete homogeneous wetting state, the Wenzel regimen can be defined as follows [50]:

$$\cos\theta_W = r\cos\theta_Y = \left(1 + 2\frac{H}{D}\right)\cos\theta_Y,$$
$$r = \frac{real\ contact\ area}{projection\ area} \approx \frac{D+2H}{D} = 1 + \frac{2H}{D} \quad (1)$$

$r$ is the roughness ratio on a patterned surface, D is the pitch distance between microstructures, and H is the height of microstructures. The curved microstructure presented in this study was simplified as a pillar structure. The width of the microstructure can be ignored because it was relatively small compared to the pitch distance. When the droplet was in a heterogeneous wetting state on microstructure, the Cassie-Baxter regimen can be defined as follows [51]:

$$\cos\theta_{CB} = f(\cos\theta_Y + 1) - 1 = \frac{A}{D}(\cos\theta_Y + 1) - 1, f = \frac{real\ contact\ area}{projection\ area} \approx \frac{A}{D} \quad (2)$$

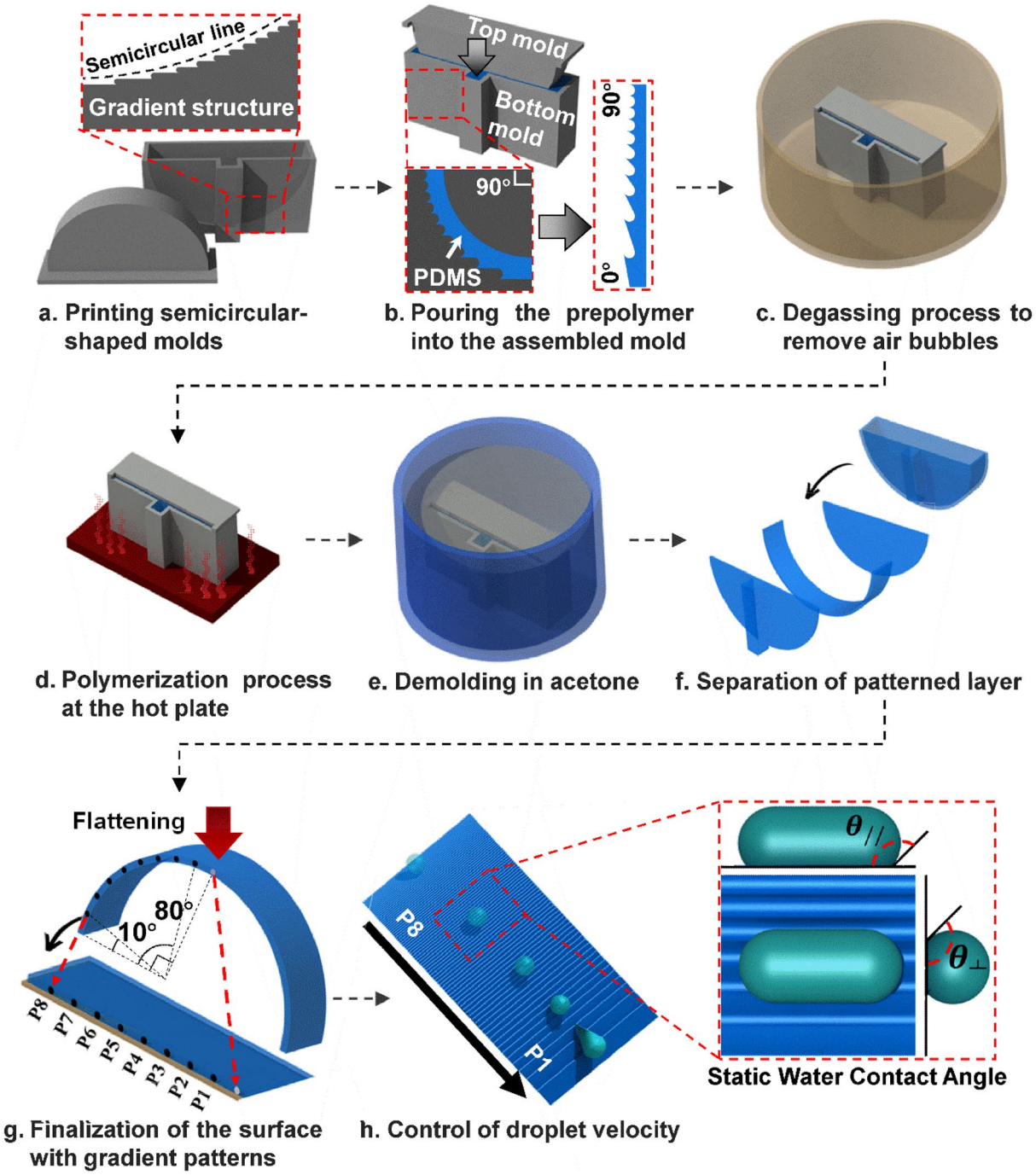


**Fig. 1** Schematic of the overall functional polymer surface creation using a 3D-printed mold. **a** Fabrication of semicircular-shaped top and bottom molds, **b** pouring the prepolymer onto the bottom mold and inserting the top mold, **c** removing air bubbles by degassing process, **d** polymerization process on the hot plate, **e** demolding in acetone, **f** separation of patterned layer by cutting the side surfaces, **g** finalization of the functional polymer surface by flattening process, and **h** control of the droplet velocity on the fabricated surface

$f$ is the ratio of the contact area to the whole projection area, and A is a real contact area on microstructures. D, H, and A in above Eqs. (1) and (2) were experimentally measured from captured images.

### 2.2.2 Droplet Velocity Test

To measure the droplet velocity on the gradient surface, ~ 12-μl droplets were released immediately above the

edge of the fabricated surface, which was inclined at 60°. Images were captured at 240 fps, and the velocity was calculated using an image analysis program (Tracker). For a comparison of the surface properties and wettability of the manufactured specimen, a surface cast was created from a mold printed with a printing angle of 80° (denoted by A80). The A80 surface was assumed to exhibit consistent wettability and was utilized to compare the droplet speed with that of the gradient-patterned fabricated surfaces. The droplet velocity at each position was measured at least five times to obtain reliable wettability data.

#### 2.2.3 Droplet Splash Test

To prove the additional effect of velocity control on the functional surface, a droplet splash test was performed on an 80°-inclined surface. Five water drops were released onto the same location on the specimen, and the distance (the horizontal distance from the tip of the surface) of the main droplet and the distance of the splash droplet were measured consecutively as they fell onto the ground. The distance of the main drop refers to the horizontal distance to the largest drop on the ground from the tip of the surface, and that of the splashed drop refers to the horizontal distance to the farthest splashed drop from the tip of the surface. The A80 surface and the flat PDMS surface were compared with the VCS.

## 3 Results and Discussion

Figure 2 presents the water contact angles at each position (P1–P8) on the fabricated surfaces of each semicircular cast with radii R3, R4, and R5, representing radii of 3, 4, and 5 cm, respectively. The perpendicular WCA ($\theta_{\perp}$) gradually increased with increasing position from P1 to P8, regardless of the radius of the semicircular cast. Hydrophobicity was observed on all areas of the VCS. At position P1, the WCAs for R3, R4, and R5 surfaces were measured to be 103.2º, 107.2º, and 93.3º, respectively. These values were different with the WCA of bare PDMS (approximately 107º [49]) because microstructures with different pitch distances were present at position P1, resulting in different contact areas between the water and surface. At positions P7 and P8, the WCA was greater than 150° for semicircular casts of all radii; in particular, at P7, the WCAs were measured to be 150.35°, 152.16°, and 151.96° for radii of 3, 4, and 5 cm, respectively, indicating superhydrophobicity. Therefore, a wettability gradient from hydrophobicity (P1–P6) to superhydrophobicity (P7 and P8) appeared along the VCS. This result shows that different WCAs (wettability) were achieved on the same surface by using a semicircular geometry that had different microstructure tilt angles (see inset of Fig. 1b). The parallel WCA ($\theta_{//}$) also gradually increased from P1 to P4 regardless of the radius, but kept similar values from P5 to P8. A continuous wettability gradient of $\theta_{\perp}$ was observed for the VCS cast from the mold with all radii. However,

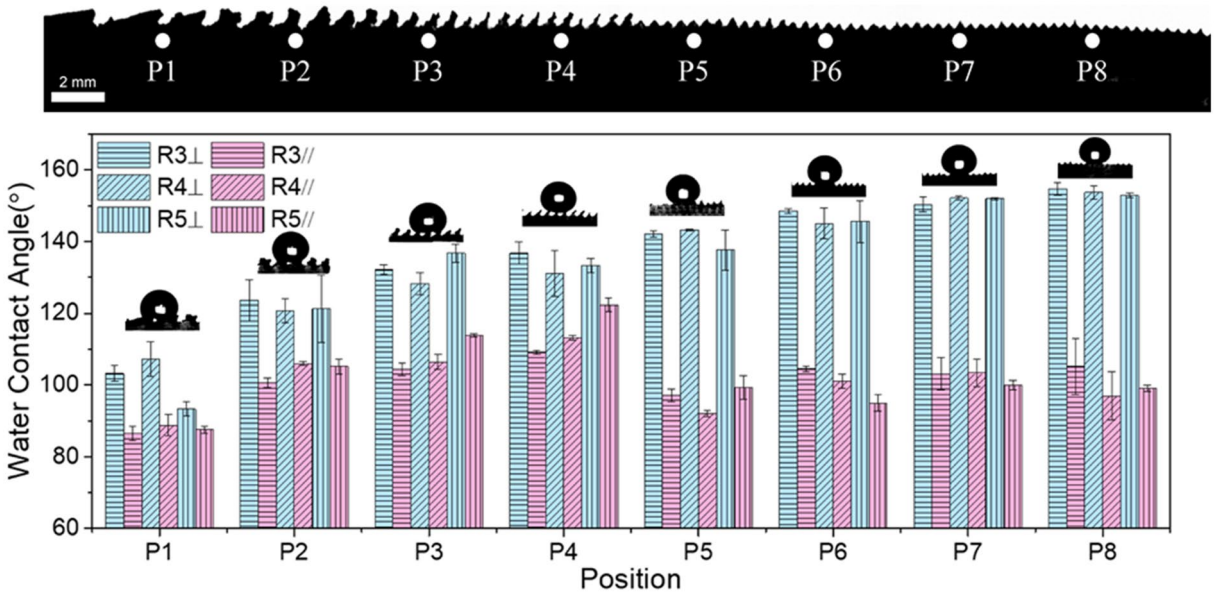


**Fig. 2** Comparison of the water contact angles at positions P1–P8 with respect to the radius of the semicircular mold. Top image: the side view of the VCS with the gradient microstructures cast from the semicircular mold with a 3-cm radius

among the three semicircular surfaces, the VCS cast from the mold with a 3-cm radius exhibited the most stable and continuous wettability gradient with a small deviation, as shown in the top image of Fig. 2. This was because the larger the radius, the more errors and non-uniformity occur in the semicircular mold during the output conversion process by the FDM-type 3D printer and flattening process. Thus, the VCS cast from the mold with a 3-cm radius was adopted for further tests and velocity measurements.

Figure 3 illustrates the tilted angle of the waveform microstructures at each position on the VCS, where the tilted angle of the microstructures increased linearly with increasing position from P1 to P8. Further, the larger the tilted angle, the greater the contact angle, as shown in Fig. 2. It should be noted that microstructures with varied angles were easily constructed using a one-step printing method. This means that the wettability of a single surface, which is highly dependent on the surface roughness, can be easily modified without multiple manufacturing processes. In other words, the height, tilted angle, length, and pitch distance of the microstructures can be readily controlled by changing the printing resolution and radius of the semicircular mold.

Figure 4 shows the height, pitch distance, and aspect ratio of microstructures with respect to the positions. The dimension of microstructure was averaged using three structures adjacent to each position. The pitch distance gradually decreased as the position moved from P1 to P8. On the other hand, the height of the microstructure increased up to P4 and decreased sharply after P5 (see Fig. 4a). The aspect ratio (a ratio of microstructure height to the pitch distance) was calculated using the measured dimension, as shown in Fig. 4b. The aspect ratio also showed a rapid change between P4 and P5, indicating that there might be two different wetting states along the VCS.

Figure 5 shows the comparison of the measured $\theta_{\perp}$ and the values calculated using the Cassie-Baxter and Wenzel equations. It was noteworthy that the wetting state along the VCS showed two different states based on the water droplet images on the surface, that is, Cassie-Baxter state from P1 to P4 and Wenzel state from P5 to P8, as shown in inset images in Fig. 5. This phenomenon was closely related to

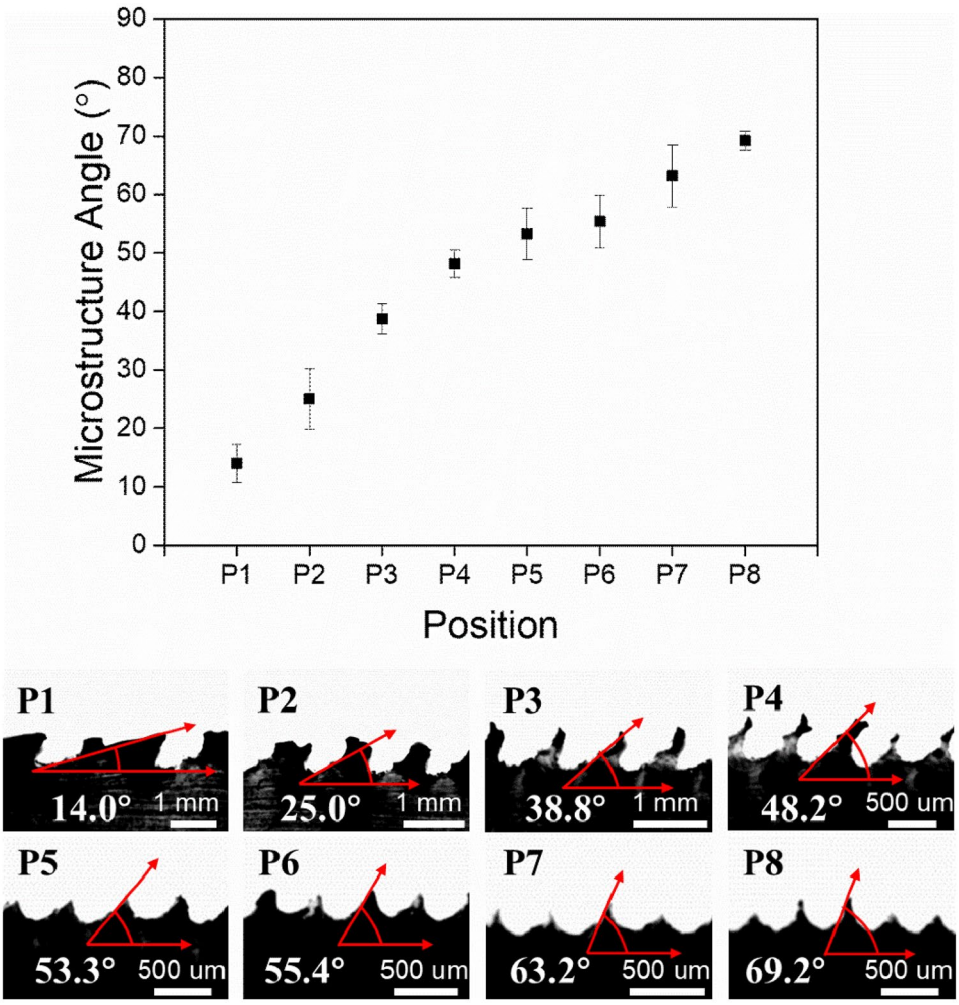


**Fig. 3** Tilted angle of microstructures at each position on the VCS. It should be noted that the angle of the microstructure changes linearly, inducing the variation in wettability

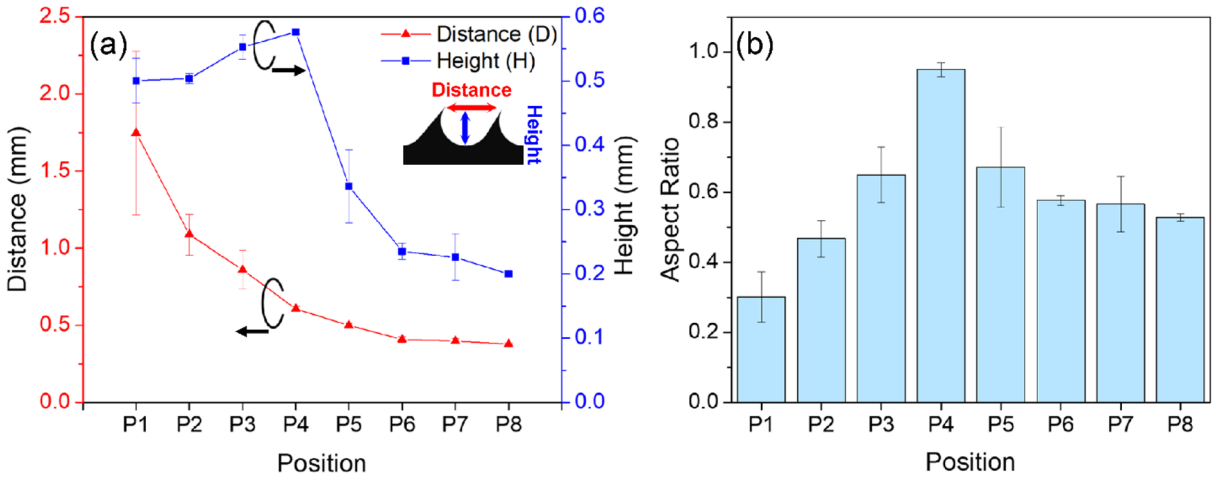


**Fig. 4** **a** Height, pitch distance, and **b** aspect ratio (=structure height/distance) of microstructures with respect to the positions

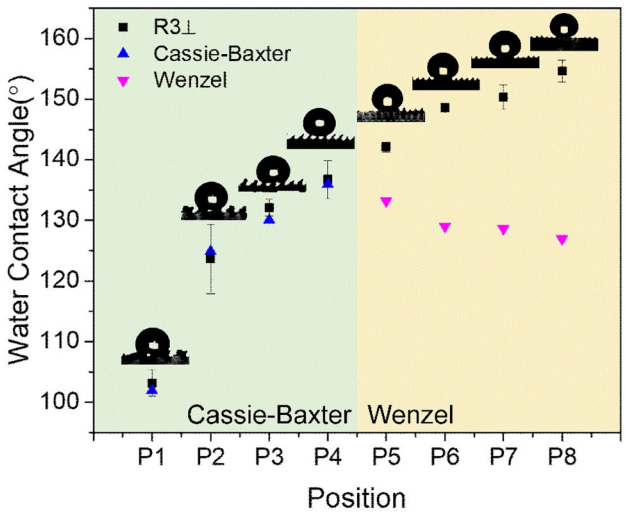


**Fig. 5** Comparison of the perpendicular WCA on the 3-cm radius VCS and values calculated using Cassie–Baxter and Wenzel regimen

the high aspect ratio and tilted angle of waveform microstructures. The high aspect ratio (see Fig. 4b) or waveform at tilted angles smaller than 50º (see Fig. 3) could prevent the water droplets from wetting but leaving them floating on the microstructure, thus indicating the Cassie–Baxter regimen. When the measured $\theta_{\perp}$ was compared with theoretical WCAs calculated using Eqs. (1) and (2), the Cassie–Baxter regimen showed a good agreement while the Wenzel regimen showed a large deviation. This means that the WCA of droplets with anisotropic wetting cannot be completely analyzed using traditional models, which was also reported in previous studies [52, 53] and needs to be further studied.

Figure 6 shows the correlation between WCA and contact length (CL). For anisotropic wettability, when the droplet size is fixed, the WCA increases as the CL decreases [54]. To verify the different WCAs at different positions from P1 to P8, the CL was measured at each position along both perpendicular and parallel directions, as shown in Fig. 6. This was because that when the number of microstructures in contact with the water droplet remained constant, the CL became decreased as the pitch distance between microstructures decreased, as shown in Fig. 4a. This opposite tendency between CL and WCA was also found in parallel direction, as shown in Fig. 6b. Compared to WCAs in the perpendicular direction, WCAs along the parallel direction did not continuously increase, indicating that the pitch distance between microstructures more affected the CL along the perpendicular direction, and thus WCAs in that direction.

Figure 7 shows the experimental setup for the droplet velocity test. The droplets were released at the same location using a fixed syringe, and the VCS was placed on a substrate tilted at 60° such that water droplets could flow over the entire surface. The axis was set at the edge of the specimen, and the velocity was measured based on the droplet's motion as it passed through each position, P1–P8, as shown in Fig. 7. To verify the performance of the manufactured specimen, the velocity of the droplet on the A80 surface was also measured simultaneously. The A80 surface was chosen for its consistent microstructure tilt angle of approximately 70º.

Figure 8 shows the velocity of the droplet on the VCS and A80 surfaces. The length of the fabricated specimen was 45 mm. The WCA of the A80 surface indicated superhydrophobicity throughout the surface; thus, the speed of the water droplets gradually increased, as shown in Fig. 8. Additionally, the coefficient of determination ($R^2$) of the linear fitting curve was approximately 0.93, indicating that the droplets fell with constant acceleration. In contrast, the droplets on the VCS with a wettability gradient initially accelerated and then gradually decelerated, presented by a quadratic

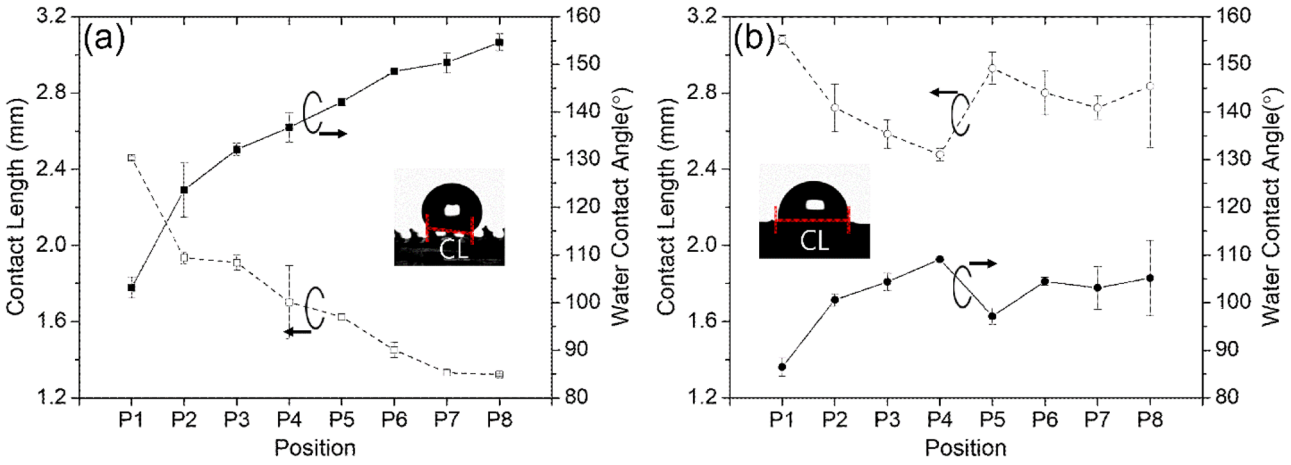


**Fig. 6** Contact length and water contact angle (**a** perpendicular and **b** parallel) with respect to positions

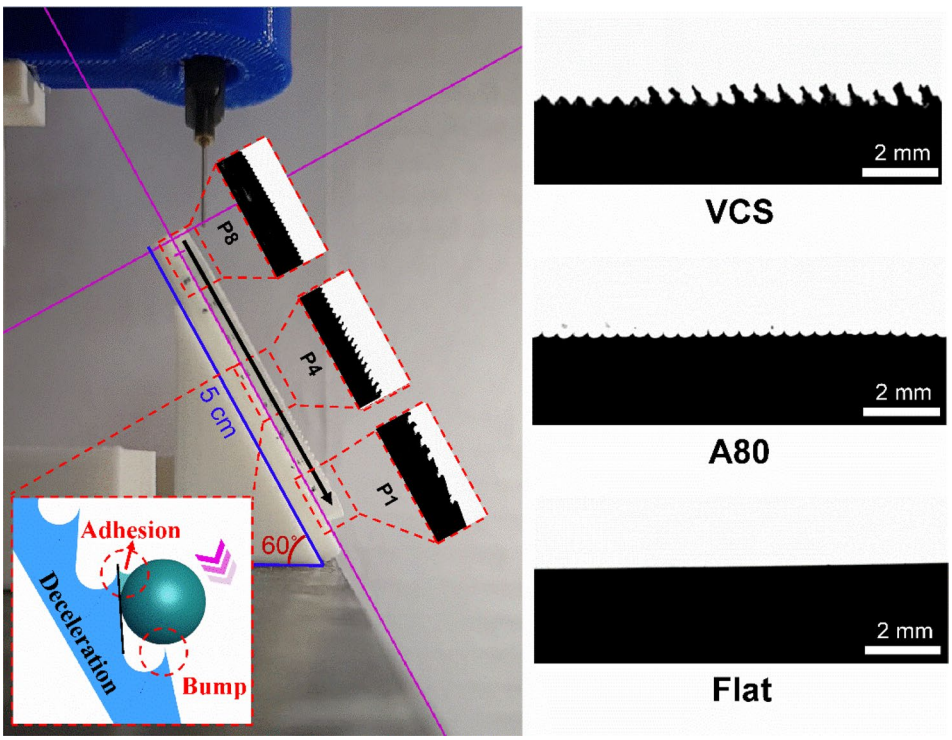


**Fig. 7** Experimental setup for the droplet velocity test with three different types of surfaces

function, and the $R^2$ of the polynomial fitting curve was approximately 0.85. On the VCS, the droplet was initially accelerated by gravitational acceleration with small friction by the low wettability (high WCA) and the small contact area. However, as the droplet passed through P4, the droplet was decelerated by the increased adhesion with decreased WCA due to the large contact area. In addition, the wave-form microstructures, which were tilted toward the opposite direction with the rolling direction of droplet, disturbed the rolling motion of droplet, thus inducing the deceleration of the droplet, as shown in the inset image of Fig. 7.

Figure 9 shows the behavior of the water droplets depending on their position on the VCS. Since position P1 had a higher wettability than other positions, the water droplets were adhesive and did not flow. Flowing or adhering based on the direction of a surface is a key characteristic of a butterfly wing [55]; therefore, this indicates that 3D-printed VCSs with wettability gradients can mimic the characteristics of butterfly wings. Furthermore, these features can be manufactured on surfaces of various scales and hence can be utilized in many engineering fields.

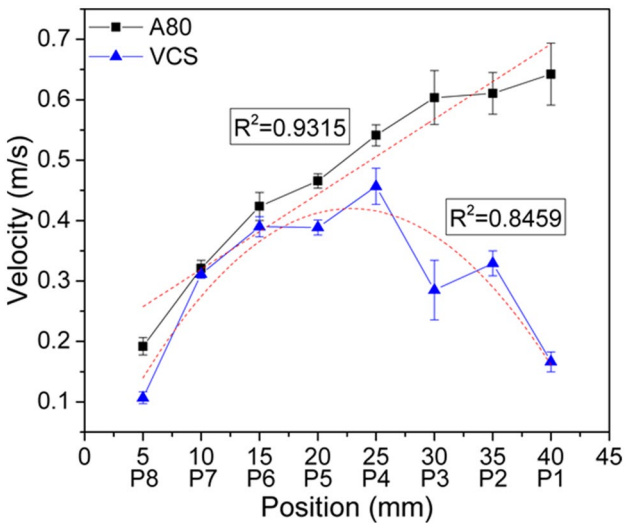


**Fig. 8** Droplet velocity along the same P1–P8 positions on the VCS and A80 surfaces

For practical application of the VCS, Fig. 10 shows a schematic of the splash test: the experiment used to verify the effect of the VCS on the flow of droplets. To prevent water droplets from flowing along the wall, the specimen was installed 2 cm from the wall; the test was conducted at the height of 43 cm to provide the rolling droplets with sufficient potential energy, and the volume of the water droplets was 12 µl. The inset image of Fig. 10 shows the measured positions of the main drop and splash drop for the A80 surface, where the distance of the fallen droplet was measured from the wall. Blue dye was added to the experiment to better identify the location of the droplet.

Figure 11 shows sequential images of a water droplet released onto the 80° tilted substrates of the VCS, A80, and flat surface with no microstructures. The water droplet rolling down the VCS finally stopped at the edge of the surface, as shown in Fig. 11a, whereas the droplet on the A80 surface fell on the ground with a high velocity, as shown in Fig. 11b, and the water droplet immediately adhered to the flat surface, as shown in Fig. 11c. This implies that, regardless of a large substrate inclination angle, only the VCS controlled the velocity of the droplet. The deceleration effects of the water droplet on the VCS are quantitatively demonstrated in Fig. 12. The splashed distance of the droplet on the flat PDMS could not be measured because the water droplets adhered to the surface and did not fall off. The distance of the main drop on the A80 surface was measured to be 8.1 cm, which was 6.1 cm away from the tip of the specimen. The horizontal distance of the splash drop from the tip of the surface due to a collision with the main drop was 20.8 cm, which was much farther than the distance of the main drop. The distances of the main drop and the splash drop from the baseline (tip of the specimen) were 6.1 and 18.8 cm, respectively, and the splash drop bounced three times as far as the main drop. However, for the VCS, the distance from the baseline to the main drop was 0.2 cm, a position very close to the baseline, and the splash drop distance was 4.3 cm, a position 2.3 cm from the baseline. Compared to that of the A80 surface, the distances of the main drop and the splash drop from the VCS specimen were reduced by 72.8% (from 8.1 to 2.2 cm) and 79.3% (from 20.8 to 4.3 cm), respectively. Moreover, when considering the baseline, the distance of the main drop and the splash drop was reduced by 96.7% (from 6.1 to 0.2 cm) and 87.8% (from 18.8 to 2.3 cm), respectively.

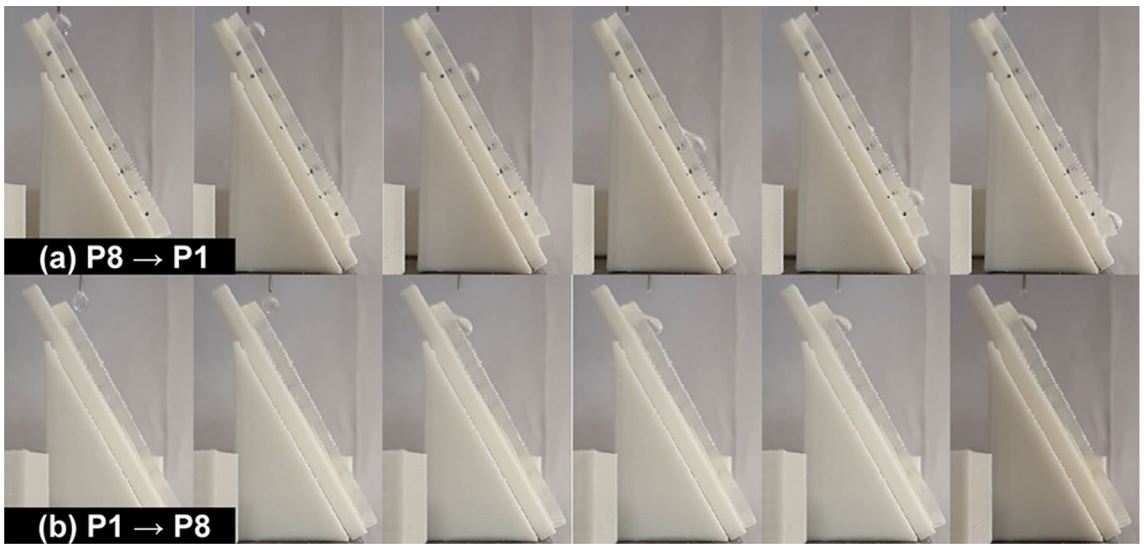


**Fig. 9** Sequential images of a water droplet on the 60°-tilted VCS flowing in **a** the flow direction (from P8 to P1) and **b** the adhesive direction (from P1 to P8)

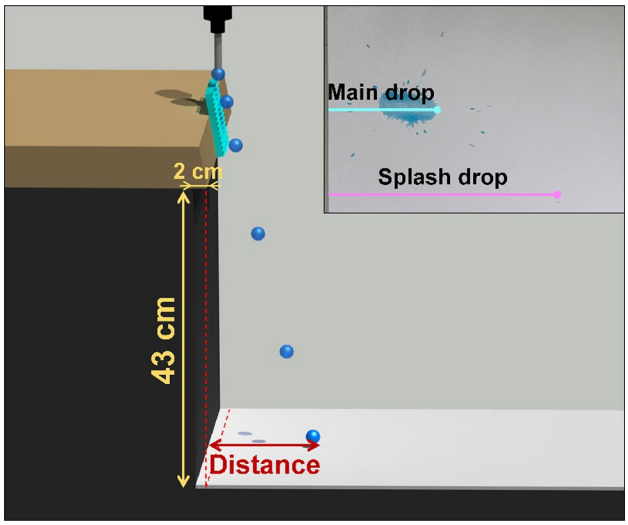


**Fig. 10** Schematic of the experimental setup for the droplet splash test. The inset image shows the distance of the main drop and the splash drop measured during the test

Thus, the VCS was shown to minimize the falling velocity by controlling the motion of the water droplet, and these tests demonstrated that it was possible to control the landing positions of the main droplet and the splash droplet on the ground. This feature could be used to minimize the impact of water droplets on the ground and hence reduce the fluctuation of liquid surfaces to obtain precise and reliable data during processes such as liquid level measurements. Thus, simple, cost-effective, and controllable polymer surfaces with wettability gradients were fabricated using 3D printing.

## 4 Conclusions

A polymer surface with varied wettability was constructed using the geometry of a 3D-printed semicircular mold. Continuously changing the microstructure on the semicircular mold during production resulted in different WCAs across various surface positions, which could be used to control the velocity of the applied droplets. The velocity experiment and analysis confirmed that a droplet released onto the VCS initially accelerated, then gradually decelerated, and finally stopped at the edge of the surface. However, when the direction of the surface was reversed, the droplet completely adhered to the surface and did not fall off. Through a rolling test along different surface directions, the characteristics of adhesion or flow were observed, similar to the characteristics of butterfly wings. For the continuous drop test using consecutive water droplets, the distance of the main drop and splash drop along the VCS was reduced by 96.7% and 87.8%, respectively, compared to the A80 surface

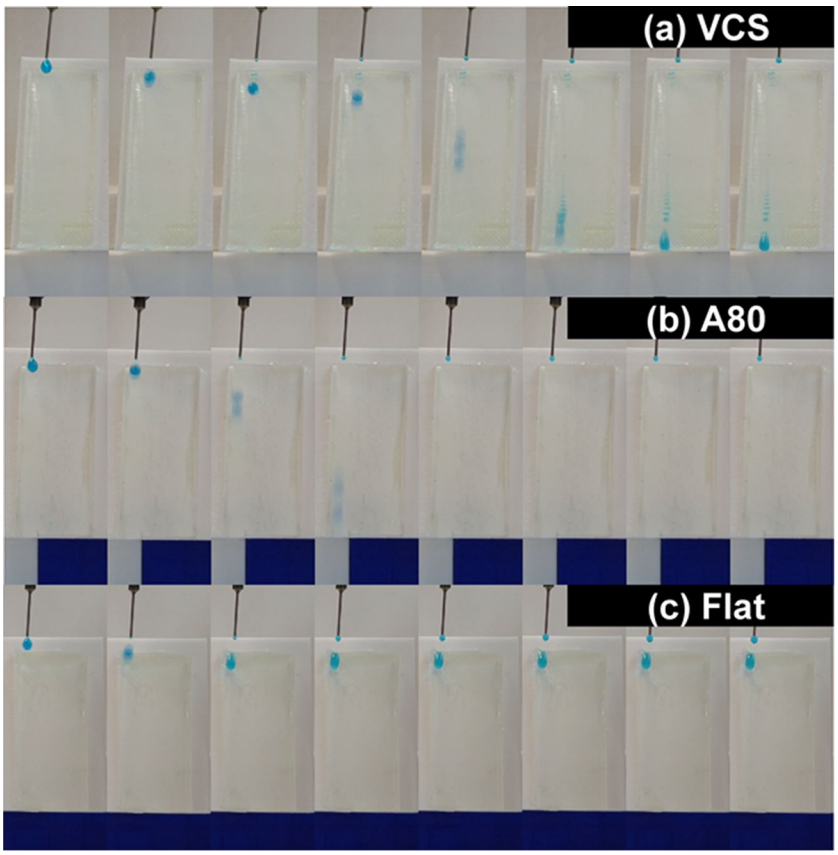


**Fig. 11** Sequential images of a water droplet flowing on the 80°-tilted **a** VCS, **b** A80, and **c** flat surface without microstructures. The real-time video can be accessed from Supplementary Video

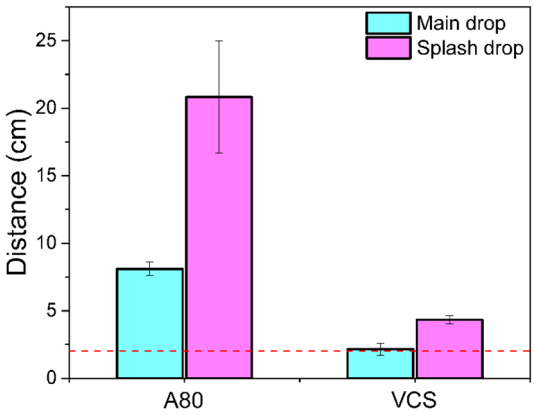


**Fig. 12** Distances of main drop and splash drop with respect to surface type

with uniform microstructure patterns. This study demonstrates the use of FDM-type 3D printing for simple, rapid, and cost-effective manufacturing of functional surfaces that decelerate water droplets. By adjusting the printing angle, the wettability gradients of the surfaces can be altered, which can then be used to control the velocity of droplets on these surfaces. This creates a smooth flow of droplets, minimizing their impact on the ground or liquid surface to reduce fluctuation and splashing. The findings of this study will facilitate the use of wettability gradient surfaces for various environmental and energy systems where a speed of rolling droplet needs to be controlled, such as desalination systems, fog harvesting structures, and hydropower plants, to improve the operating efficiency by minimizing water loss due to droplet splashing.

**Supplementary Information** The online version contains supplementary material available at https://doi.org/10.1007/s40684-022-00418-y.

**Acknowledgements** This work was supported by a National Research Foundation of Korea (NRF) grant funded by the Korean government (MSIT) (No. NRF-2020R1A4A1019074).

## Declarations

**Conflict of interest** There are no conflicts to declare.

## References

1. Ensikat, H. J., Ditsche-Kuru, P., Neinhuis, C., & Barthlott, W. (2011). Superhydrophobicity in perfection: The outstanding properties of the lotus leaf. *Beilstein Journal of Nanotechnology, 2,* 152–161.
2. Latthe, S. S., Terashima, C., Nakata, K., & Fujishima, A. (2014). Superhydrophobic surfaces developed by mimicking hierarchical surface morphology of lotus leaf. *Molecules, 19,* 4256–4283.
3. Bhushan, B., & Her, E. K. (2010). Fabrication of superhydrophobic surfaces with high and low adhesion inspired from rose petal. *Langmuir, 26,* 8207–8217.
4. Feng, L., Zhang, Y., Xi, J., Zhu, Y., Wang, N., Xia, F., & Jiang, L. (2008). Petal effect: A superhydrophobic state with high adhesive force. *Langmuir, 24,* 4114–4119.
5. Oeffner, J., & Lauder, G. V. (2012). The hydrodynamic function of shark skin and two biomimetic applications. *The Journal of Experimental Biology, 215,* 785–795.
6. Wen, L., Weaver, J. C., & Lauder, G. V. (2014). Biomimetic shark skin: Design, fabrication and hydrodynamic function. *The Journal of Experimental Biology, 217,* 1656–1666.
7. Gu, Z. Z., Uetsuka, H., Takahashi, K., Nakajima, R., Onishi, H., Fujishima, A., & Sato, O. (2003). Structural color and the lotus effect. *Angewandte Chemie International Edition,* 42, 894–897.
8. Seo, K., Wober, M., Steinvurzel, P., Schonbrun, E., Dan, Y., Ellenbogen, T., & Crozier, K. B. (2011). Multicolored vertical silicon nanowires. *Nano Letters, 11,* 1851–1856.
9. Ma, M., & Hill, R. M. (2006). Superhydrophobic surfaces. *Current Opinion in Colloid & Interface Science, 11,* 193–202.
10. Onda, T., Shibuichi, S., Satoh, N., & Tsujii, K. (1996). Super-water-repellent fractal surfaces. *Langmuir, 12*, 2125.
11. Tian, P., & Guo, Z. (2017). Bioinspired silica-based superhydrophobic materials. *Applied Surface Science, 426,* 1–18.
12. Singh, A. K., & Singh, J. K. (2019). An efficient use of waste PE for hydrophobic surface coating and its application on cotton fibers for oil-water separator. *Progress in Organic Coatings, 131,* 301–310.
13. Kooij, E. S., Jansen, H. P., Bliznyuk, O., Poelsema, B., & Zandvliet, H. J. W. (2012). Directional wetting on chemically patterned substrates. *Colloids and Surfaces A: Physicochemical and engineering Aspects, 413,* 328–333.
14. Chowdhury, I. U., Sinha Mahapatra, P., & Sen, A. K. (2019). Self-driven droplet transport: Effect of wettability gradient and confinement. *Physics of Fluids, 31,* 1–12.
15. Nakashima, Y., Nakanishi, Y., & Yasuda, T. (2015). Automatic droplet transportation on a plastic microfluidic device having wettability gradient surface. *The Review of Scientific Instruments, 86,* 1–6.
16. Lee, J. H., Khang, G., Lee, J. W., & Lee, H. B. (1998). Interaction of different types of cells on polymer surfaces with wettability gradient. *Journal of Colloid and Interface Science, 205,* 323–330.
17. Kim, M. S., Khang, G., & Lee, H. B. (2008). Gradient polymer surfaces for biomedical applications. *Progress in Polymer Science, 33,* 138–164.
18. Sun, C., Zhao, X. W., Han, Y. H., & Gu, Z. Z. (2008). Control of water droplet motion by alteration of roughness gradient on silicon wafer by laser surface treatment. *Thin Solid Films, 516,* 4059–4063.
19. Wang, X., Xu, B., Chen, Y., Ma, C., & Huang, Y. (2019). Fabrication of micro/nano-hierarchical structures for droplet manipulation via velocity-controlled picosecond laser surface texturing. *Optics and Lasers in Engineering, 122,* 319–327.
20. Qi, L., Niu, Y., Ruck, C., & Zhao, Y. (2019). Mechanical-activated digital microfluidics with gradient surface wettability. *Lab on a Chip, 19,* 223–232.
21. Morgenthaler, S., Lee, S., Zürcher, S., & Spencer, N. D. (2003). A simple, reproducible approach to the preparation of surface-chemical gradients. *Langmuir, 19,* 10459–10462.
22. Liao, Q., Wang, H., Zhu, X., & Li, M. (2006). Liquid droplet movement on horizontal surface with gradient surface energy. *Science in China Series E: Technological Sciences, 49,* 733–741.
23. Zhang, G., Zhang, X., Li, M., & Su, Z. (2014). A surface with superoleophilic-to-superoleophobic wettability gradient. *ACS Applied Materials & Interfaces, 6,* 1729–1733.

24. Zhang, J., & Han, Y. (2008). A topography/chemical composition gradient polystyrene surface: Toward the investigation of the relationship between surface wettability and surface structure and chemical composition. *Langmuir, 24,* 796–801.
25. Zhao, N., Li, M., Gong, H., & Bai, H. (2020). Controlling ice formation on gradient wettability surface for high-performance bioinspired materials. *Science Advances, 6,* 1–10.
26. Liu, H., Xu, J., Li, Y., Li, B., Jun, M., & Zhang, X. (2006). Fabrication and characterization of an organic-inorganic gradient surface made by polymethylsilsesquioxane (PMSQ). *Macromolecular Rapid Communications, 27,* 1603–1607.
27. Banuprasad, T. N., Vinay, T. V., Subash, C. K., Varghese, S., George, S. D., & Varanakkottu, S. N. (2017). Fast transport of water droplets over a thermo-switchable surface using rewritable wettability gradient. *ACS Applied Materials & Interfaces, 9*, 28046–28054.
28. Yu, X., Wang, Z., Jiang, Y., & Zhang, X. (2006). Surface gradient material: From superhydrophobicity to superhydrophilicity. *Langmuir, 22,* 4483–4486.
29. Sehayek, T., Vaskevich, A., & Rubinstein, I. (2003). Preparation of graded materials by laterally controlled template synthesis. *Journal of the American Chemical Society, 125,* 4718–4719.
30. Liu, C., Sun, J., Li, J., Xiang, C., Che, L., Wang, Z., & Zhou, X. (2017). Long-range spontaneous droplet self-propulsion on wettability gradient surfaces. *Scientific Reports, 7,* 1–8.
31. Huang, D. J., & Leu, T. S. (2013). Fabrication of high wettability gradient on copper substrate. *Applied Surface Science, 280,* 25–32.
32. Tokunaga, A., & Tsuruta, T. (2020). Enhancement of condensation heat transfer on a microstructured surface with wettability gradient. *International Journal of Heat and Mass Transfer, 156,* 119839.
33. Pitt, W. G. (1989). Fabrication of a continuous wettability gradient by radio frequency plasma discharge. *Journal of Colloid and Interface Science, 133,* 223–227.
34. Ito, Y., Heydari, M., Hashimoto, A., Konno, T., Hirasawa, A., Hori, S., & Nakajima, A. (2007). The movement of a water droplet on a gradient surface prepared by photodegradation. *Langmuir, 23,* 1845–1850.
35. Daniel, S., & Chaudhury, M. K. (2002). Rectified motion of liquid drops on gradient surfaces induced by vibration. *Langmuir, 18*, 3404–3407.
36. Furet, B., Poullain, P., & Garnier, S. (2019). 3D printing for construction based on a complex wall of polymer-foam and concrete. *Additive Manufacturing, 28,* 58–64.
37. Vyatskikh, A., Delalande, S., Kudo, A., Zhang, X., Portela, C. M., & Greer, J. R. (2018). Additive manufacturing of 3D nano-architected metals. *Nature Communiations, 9,* 1–8.
38. Buj-Corral, I., Bagheri, A., Domínguez-Fernández, A., & Casado-López, R. (2019). Influence of infill and nozzle diameter on porosity of FDM printed parts with rectilinear grid pattern. *Procedia Manufacturing, 41,* 288–295.
39. Sukindar, N. A., Ariffin, M. K. A., Hang Tuah Baharudin, B. T., Jaafar, C. N. A., & Ismail, M. I. S. (2016). Analyzing the effect of nozzle diameter in fused deposition modeling for extruding polylactic acid using open source 3D printing. *Journal of Teknol, 78,* 7–15.
40. Shin, S., & So, H. (2020). Effect of 3D printing raster angle on reversible thermo-responsive composites using PLA/Paper bilayer. *Smart Materials and Structures, 29,* 105016.
41. Sung, J., & So, H. (2021). 3D printing-assisted fabrication of microgrid patterns for flexible antiadhesive polymer surfaces. *Surfaces and Interfaces, 23,* 100935.
42. Ding, S., Zou, B., Wang, P., & Ding, H. (2019). Effects of nozzle temperature and building orientation on mechanical properties and microstructure of PEEK and PEI printed by 3D-FDM. *Polymer Testing, 78,* 105948.
43. Alsoufi, M. S., Alhazmi, M. W., Suker, D. K., Alghamdi, T. A., Sabbagh, R. A., Felemban, M. A., & Bazuhair, F. K. (2019). Experimental characterization of the influence of nozzle temperature in FDM 3D printed pure PLA and advanced PLA+. *American Journal of Mechanical Engineering, 7,* 45–60.
44. Akhoundi, B., Nabipour, M., Hajami, F., & Shakoori, D. (2020). An experimental study of nozzle temperature and heat treatment (Annealing) effects on mechanical properties of high-temperature polylactic acid in fused deposition modeling. *Polymer Engineering and Science, 60,* 979–987.
45. Kang, B., Hyeon, J., & So, H. (2020). Facile microfabrication of 3-dimensional (3D) hydrophobic polymer surfaces using 3D printing technology. *Applied Surface Science, 499,* 143733.
46. Kang, B., Sung, J., & So, H. (2021). Realization of superhydrophobic surfaces based on three-dimensional printing technology. *International Journal of Precision Engineering and Manufacturing-Green Technology, 8*(1), 47–55.
47. Xu, Z., & Lü, F. (2013). A static contact angle algorithm and its application to hydrophobicity measurement in silicone rubber corona aging test. *IEEE Transactions on Dielectrics and Electrical Insulation, 20,* 1820–1831.
48. Ali, M., & Hackam, R. (2008). Effects of saline water and temperature on surface properties of HTV silicone rubber. *IEEE Transactions on Dielectrics and Electrical Insulation, 15,* 1368–1378.
49. Ruben, B., Elisa, M., Leandro, L., Victor, M., Gloria, G., Marina, S., & Nadhira, L. (2017). Oxygen plasma treatments of polydimethylsiloxane surfaces: effect of the atomic oxygen on capillary flow in the microchannels. *Micro & Nano Letters, 12,* 754–757.
50. Wenzel, R. N. (1936). Resistance of solid surfaces to wetting by water. *Industrial and Engineering Chemistry, 28,* 988–994.
51. Cassie, A. B. D., & Baxter, S. (1944). Wettability of porous surfaces. *Transactions of the Faraday Society, 40,* 546–551.
52. Faria-Briceno, J. J., Neumann, A., Schunk, P. R., & Brueck, S. R. J. (2019). Measuring liquid drop properties on nanoscale 1D patterned photoresist structures. *Scientific Reports, 9,* 1–9.
53. Cheng, C. T., To, S., & Zhang, G. (2020). Characterization of intermediate wetting states on micro-grooves by water droplet contact line. *Journal of Industrial and Engineering Chemistry, 91,* 69–78.
54. Xu, J., Hou, Y., Lian, Z., Yu, Z., Wang, Z., & Yu, H. (2020). Bioinspired design of bi/tridirectionally anisotropic sliding superhydrophobic titanium alloy surfaces. *Nanomaterials, 10,* 1–17.
55. Zheng, Y., Gao, X., & Jiang, L. (2007). Directional adhesion of superhydrophobic butterfly wings. *Soft Matter, 3,* 178–182.




**Jaebum Sung** received the B.S. degree from Hanyang University, Korea, in 2019, where he is currently pursuing the M.S. and Ph.D. degrees in the Mechanical Engineering Department. His research interests include micro sensors for aeronautical applications, precision engineering, micromachining, microscale heat transfer, and thin film deposition.

**Hoo Min Lee** received his B.S. degree in Mechanical Engineering from Hanyang University, Korea, in 2019. He is currently pursuing the integrated Ph.D. course in Mechanical Engineering, Hanyang University, Korea. His research interests include thermal buckling, hyperelasticity analysis, elastomer mechanism analysis, and topology optimization.

**Gil Ho Yoon** received his B.S. degree in Mechanical and Aerospace Engineering from Seoul National University in 1998, and he received his M.S. and Ph.D. degrees in Mechanical and Aerospace Engineering from Seoul National University in 2000 and 2004, respectively. Dr. Yoon is currently a Professor at School of Mechanical Engineering, Hanyang University, Korea. His research interests include topology optimization, model order reduction, multiphysics system design, acoustic/vibration absorption analysis, and penetration analysis.

**Sungchul Bae** received the B.S. degree from Hanyang University, Korea, in 2007, the M.S. degree from the University of Tokyo, Japan, in 2010, all in the Department of Architectural Engineering, and the Ph.D. degree from the University of California, Berkeley, in 2014, in the Department of Civil and Environmental Engineering. He is currently an Associate Professor in the Department of Architectural Engineering, Hanyang University. His research interests include identifying cement nanostructures' characteristics using synchrotron technology, developing eco-friendly low-carbon cement, physical properties evaluation of cement-based materials mixed with various nanomaterials, and 3D printing cement material development.

**Hongyun So** received the B.S. degree from Hanyang University, Korea, in 2009, the M.S. degree from KAIST, Korea, in 2011, and the Ph.D. degree from the University of California, Berkeley, in 2014, all in mechanical engineering. He joined Stanford University in 2015 as a Post-Doctoral Scholar with the Aeronautics and Astronautics Department. He is currently an Assistant Professor with the Mechanical Engineering Department, Hanyang University. His research interests include design, modeling, and manufacturing of micro/nanosystems, intelligent sensors, and mechanical issues related to heat transfer and fluid mechanics.